

# A THREE-DIMENSIONAL PLASMA AND ENERGETIC PARTICLE INVESTIGATION FOR THE WIND SPACECRAFT

R. P. LIN, K. A. ANDERSON, S. ASHFORD, C. CARLSON, D. CURTIS, R. ERGUN,  
D. LARSON and J. McFADDEN

*Spaces Sciences Laboratory, University of California, Berkeley, CA 94720, U.S.A.*

M. McCARTHY and G. K. PARKS

*Geophysics Program, AK50, University of Washington, Seattle, WA 98195, U.S.A.*

H. RÈME, J. M. BOSQUED, J. COUTELIER, F. COTIN and C. D'USTON

*Centre d'Etude Spatiale des Rayonnements, Université Paul Sabatier, B.P. 4346, Toulouse, France*

K.-P. WENZEL, T. R. SANDERSON, J. HENRION and J. C. RONNET

*Space Science Department of ESA, European Space Research and Technology Centre (ESTEC),  
Noordwijk, 2200AG, The Netherlands*

and

G. PASCHMANN

*Max Planck Institut für Extraterrestrische Physik, 85740 Garching bei München, Germany*

(Received 28 January, 1993)

**Abstract.** This instrument is designed to make measurements of the full three-dimensional distribution of suprathermal electrons and ions from solar wind plasma to low energy cosmic rays, with high sensitivity, wide dynamic range, good energy and angular resolution, and high time resolution. The primary scientific goals are to explore the suprathermal particle population between the solar wind and low energy cosmic rays, to study particle acceleration and transport and wave-particle interactions, and to monitor particle input to and output from the Earth's magnetosphere.

Three arrays, each consisting of a pair of double-ended semi-conductor telescopes each with two or three closely sandwiched passivated ion implanted silicon detectors, measure electrons and ions above  $\sim 20$  keV. One side of each telescope is covered with a thin foil which absorbs ions below 400 keV, while on the other side the incoming  $<400$  keV electrons are swept away by a magnet so electrons and ions are cleanly separated. Higher energy electrons (up to  $\sim 1$  MeV) and ions (up to 11 MeV) are identified by the two double-ended telescopes which have a third detector. The telescopes provide energy resolution of  $\Delta E/E \approx 0.3$  and angular resolution of  $22.5^\circ \times 36^\circ$ , and full  $4\pi$  steradian coverage in one spin (3 s).

Top-hat symmetrical spherical section electrostatic analyzers with microchannel plate detectors are used to measure ions and electrons from  $\sim 3$  eV to 30 keV. All these analyzers have either  $180^\circ$  or  $360^\circ$  fields of view in a plane,  $\Delta E/E \approx 0.2$ , and angular resolution varying from  $5.6^\circ$  (near the ecliptic) to  $22.5^\circ$ . Full  $4\pi$  steradian coverage can be obtained in one-half or one spin. A large and a small geometric factor analyzer measure ions over the wide flux range from quiet-time suprathermal levels to intense solar wind fluxes. Similarly two analyzers are used to cover the wide range of electron fluxes. Moments of the electron and ion distributions are computed on board.

In addition, a Fast Particle Correlator combines electron data from the high sensitivity electron analyzer with plasma wave data from the WAVE experiment (Bougeret *et al.*, in this volume) to study wave-particle interactions on fast time scales. The large geometric factor electron analyzer has electrostatic deflectors to steer the field of view and follow the magnetic field to enhance the correlation measurements.

## 1. Introduction

For many years the solar wind has been regarded as a regime essentially independent from the energetic particle populations found in interplanetary space. The particles in the intervening energy range, from just above solar wind plasma to 1 MeV, are referred to here as suprathermal particles. These particles play a key role in the varied plasma and energetic particle phenomena observed to occur in the interplanetary medium (IPM) and upstream from the Earth's magnetosphere. Because of dynamic range considerations, instruments designed to measure the solar wind plasma ions and electrons lack the sensitivity to detect these suprathermal particles except during highly disturbed times. This experiment for the WIND spacecraft is designed specifically to make measurements of the three-dimensional distribution of plasma and energetic electrons and ions in the energy range a few eV to  $\geq$  several hundred keV. Figures 1 and 2 show the typical energy flux spectra of various interplanetary and distant magnetospheric particle phenomena, and the energy range and counting rates for various detectors of this instrument.

The scientific objectives of this experiment are:

- (a) The first detailed exploration of the interplanetary particle population in the suprathermal energy range.
- (b) The study of particle acceleration at the Sun, in the interplanetary medium, and upstream from the Earth.
- (c) The study of the transport of suprathermal particles in the interplanetary medium.
- (d) The study of basic plasma processes occurring in the interplanetary medium, such as wave-particle interactions, the production of radio emission by beam-plasma processes (Type III bursts), shock waves, nonlinear processes such as soliton collapse, and solar wind heat flux.
- (e) The measurement of the particle and plasma input to and output from the Earth's magnetosphere.

## 2. Scientific Objectives

### 2.1. SUPRATHERMAL ELECTRONS

On the ISEE-3 spacecraft, the University of California, Berkeley's electron electrostatic analyzer was able to make detailed measurements for the first time with high enough sensitivity to observe the normal 'quiet' interplanetary electron population down to 2 keV. Several new and important phenomena were discovered immediately:

- (1) A quiet time electron population from 2–20 keV apparently of solar origin (Lin, 1985) (Figure 1).
- (2) Impulsive solar electron events extending from  $<2$  keV to  $\sim 10$  keV which, unlike other impulsive solar particle events, were mostly not associated with an

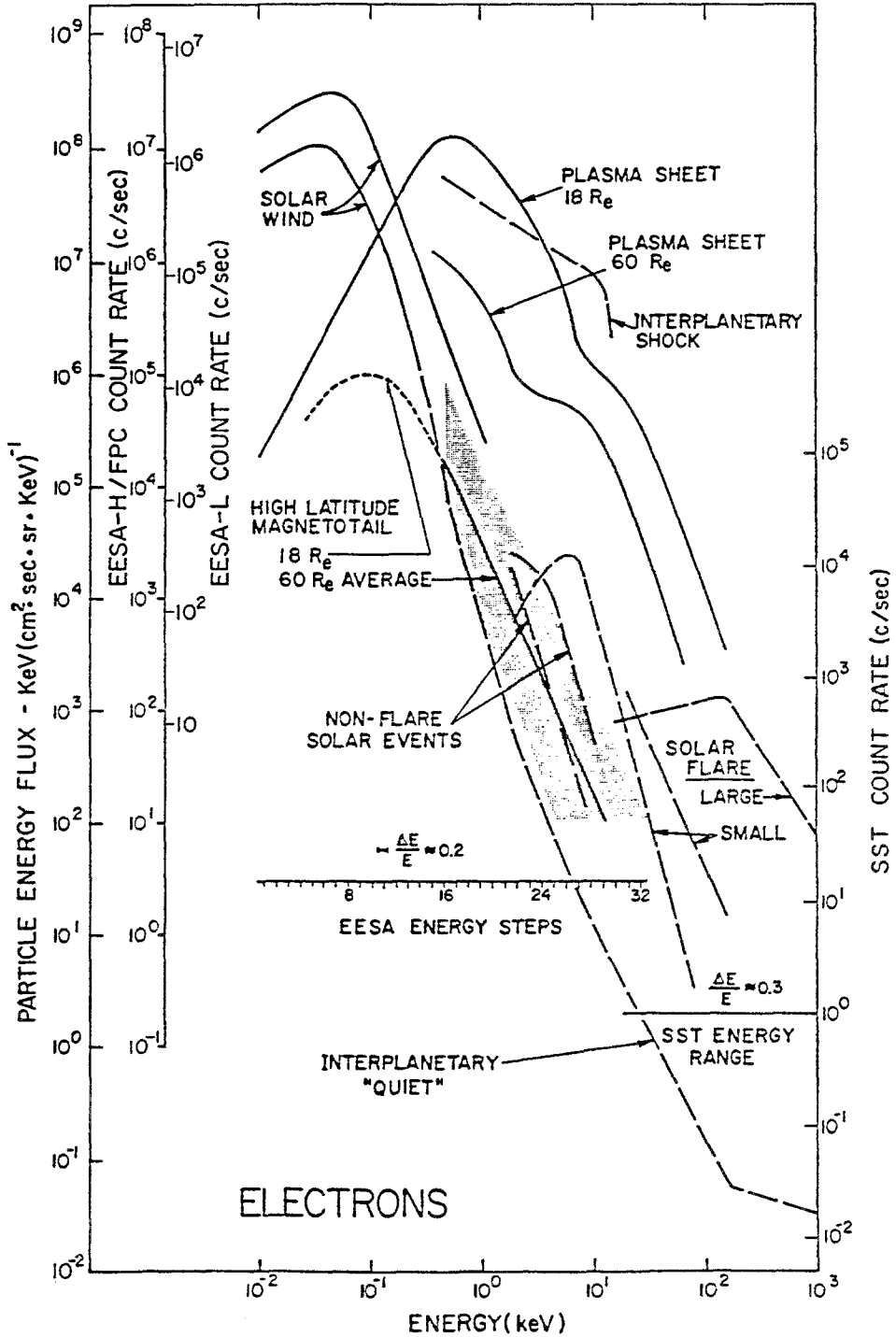


Fig. 1. Electron energy flux ( $E(dJ/dE)$ ) in the interplanetary medium and outer magnetosphere. Counting rates per channel for the EESA and SST are indicated on the left and right axes, respectively.

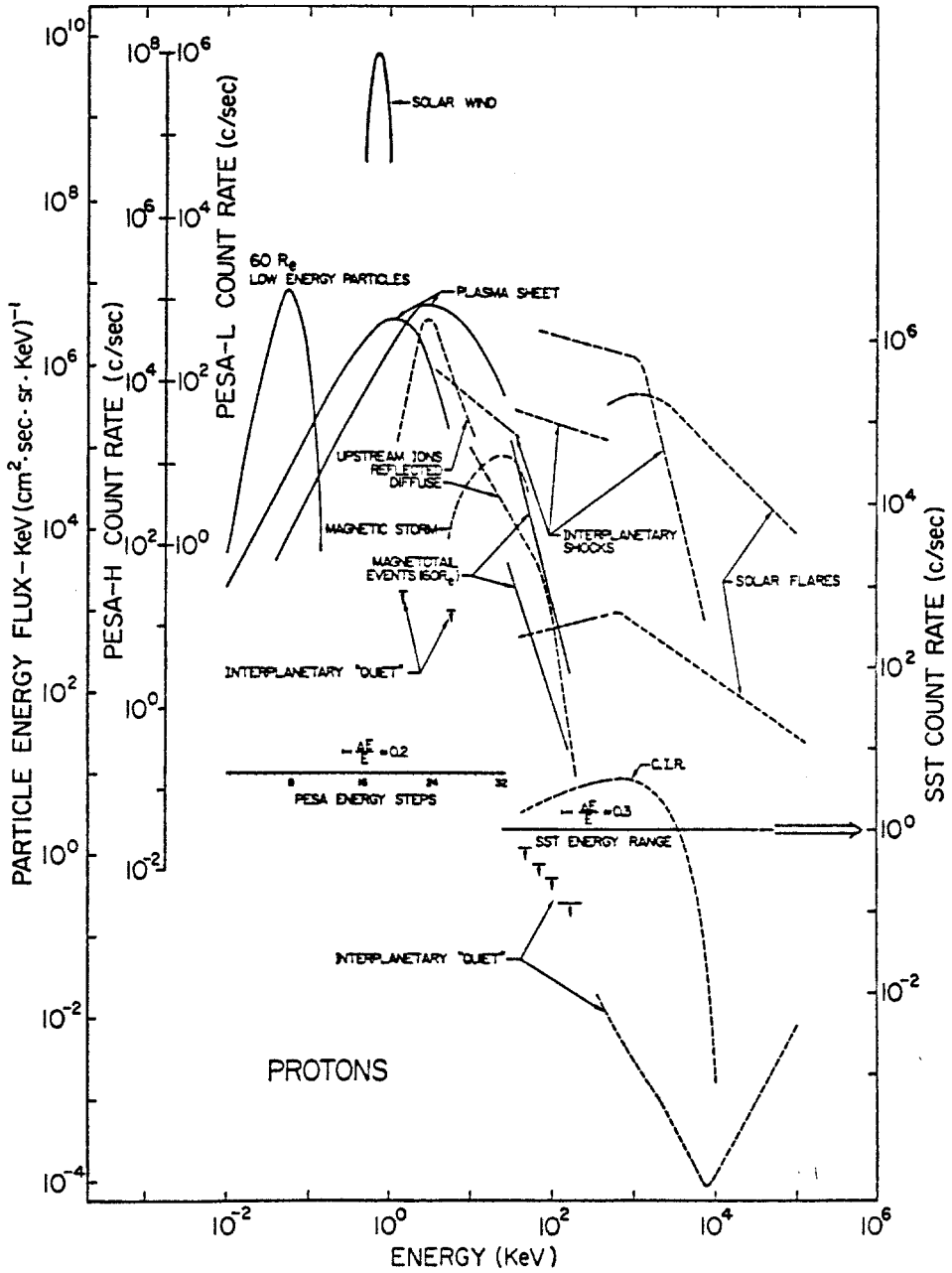


Fig. 2. Proton energy flux ( $E(dJ/dE)$ ) in the interplanetary medium and outer magnetosphere. Counting rates per channel for the PESA and SST are indicated on the left and right axes, respectively.

observed solar flare (Potter *et al.*, 1980). These events turn out to be the most common solar particle events observed.

(3) A transition in propagation properties for electrons at 10–20 keV. At low energies the propagation is always essentially scatter-free while above 20 keV it is almost always diffusive.

(4) Highly structured pitch angle distributions for  $\sim 2$ –10 keV electrons at interplanetary shocks, and in large solar flare events, possibly due to a combination of shock acceleration, magnetic reflection, and scatter-free propagation (Anderson *et al.*, 1982). These particles provide excellent long-range (several AU) probes of the heliosphere (see Lin and Kahler, 1992).

These discoveries emphasize the need for new high sensitivity measurements in unexplored energy regions. They also lead to many important questions:

(1) What is the origin of the quiet time 2–20 keV electron population? How are these particles related to the solar wind plasma electrons? If solar, what processes at the Sun could lead to such a non-thermal population? Are the waves which are hypothesized for coronal heating also accelerating these particles?

(2) What impulsive energy release process, most likely in the high corona, produces these bursts of low energy  $\lesssim 2$ –10 keV electrons? How high in the corona is this process taking place? How is it related to solar flares? Are there more impulsive events at even lower energies ( $\lesssim 2$  keV)?

(3) What causes the change in electron propagation from diffusive (scattering-dominated) to scatter-free (dominated by diverging **B**)? Is the IMF free of irregularities below  $\sim 10$  km?

(4) How are electrons accelerated by interplanetary shocks? Are these electrons the source of type II solar radio emission?

## 2.2. PARTICLE ACCELERATION, STORAGE, AND PROPAGATION AT THE SUN

Small solar flares often accelerate electrons up to  $\sim 10^2$  keV during the flash phase. In large flares, both ions and electrons are observed up to relativistic energies. The flash phase electrons may contain the bulk of energy released in the flare (Lin and Hudson, 1971, 1976).

Measurements of solar flare particles are lacking below  $\sim 10^2$  keV for ions and below  $\sim 2$  keV for electrons. The behavior of ion fluxes from  $\sim 10^2$  keV–10 MeV are highly complex, probably due to effects of propagation and interplanetary acceleration. Detailed time profiles and angular measurements will help to unravel propagation effects so as to obtain the source spectrum. Measurements to low energies are needed to define the acceleration spectrum and to indicate how much matter the particles passed through, thereby giving information on the location of the source and the amount of storage at the Sun. Comparisons with solar flare X-ray, gamma-ray, radio, and optical measurements will help answer these important questions:

What is the acceleration mechanism? Is there one acceleration process producing both the escaping particles and those which remain at the Sun to produce the hard X-rays and gamma-rays? How is the acceleration at interplanetary shocks related to that occurring at the Sun in the second stage? Are particles stored at the Sun for long periods or is there continuous acceleration? How do the particles escape? How is the flare flash phase acceleration related to the non-flare 2–10 keV electron acceleration process?

### 2.3. LANGMUIR WAVES AND RADIO BURSTS

An important problem in plasma physics and solar physics is the generation of solar radio emission. Type III solar radio bursts are produced by energetic electrons accelerated at the Sun and travelling outward through the corona and IPM. Because the faster electrons run ahead of the slower ones, a ‘bump on tail’ distribution arises which is unstable to the production of electron plasma waves. These plasma waves then produce the observed electromagnetic radiation at  $2\omega_p$  and  $\omega_p$  through scattering or some other nonlinear processes. As the electrons travel outward into lower density plasma, the radiation shows a characteristic rapid drift to lower frequencies. ISEE-3 observations have provided the first detailed measurements of the electron distribution function  $f(v_{||})$  for comparison with simultaneous plasma wave and low frequency radio burst measurements (Lin *et al.*, 1981). The plasma waves are extremely bursty, with time scales of 0.1 s, and nonlinear wave-wave interactions appear to be important (Lin *et al.*, 1986). Because of the rapid evolution of these impulsive events, the bursty nature of the waves, and the extremely narrow angular distributions of the electrons, the ISEE-3 observations are marginal for study of this plasma process, even in the largest events. With the better angular resolution, higher sensitivity and time resolution of this experiment, and with the Fast Particle Correlator (see description below) to study this process on physically appropriate time scales, we can address the following important questions:

How does the electron distribution evolve during the bursts of plasma waves? Is energy being transferred from the resonant electrons to waves and *vice versa*? Are these bursts due to strong turbulence processes such as soliton collapse?

### 2.4. SUPRATHERMAL IONS

For ions in the energy range below  $\sim 40$  keV, there are no quiet time measurements, only upper limits at 1.5 and 6 keV from ISEE-1 and -2 experiments whose detectors look perpendicular to the ecliptic plane, and a few tantalizing observations of shock accelerated ions (Gosling *et al.*, 1980) and magnetic storm ions (Frank, 1969). But measurements in this range are very important because the energy density of these particles could easily dominate the plasma in the frame of the solar wind. Also the quiet suprathermal ion population may provide the source of the particles accelerated to produce the shock associated and storm ions, and the

higher energy ( $>40$  keV) quiet time populations. Furthermore, measurements of the quiet suprathermal ions will give information on acceleration processes in the solar wind and at the Sun.

The few available measurements in the 200 keV to 10 MeV ion range show this population to be highly variable. Some of this variability is certainly due to the solar origin of many of these particles. Also flux increases are observed in association with solar wind fast stream-slow stream corotating interaction regions (CIR) (Barnes and Simpson, 1976; Gloeckler *et al.*, 1979) even at solar quiet times. However, there appears to be a minimum level below which these fluxes never fall. These particles may have an origin quite different from the flare, active region, and CIR particles. Here accumulation of data over a considerable portion of a solar cycle is necessary, as is measurement of the energy spectrum over a wide range, extending from solar wind to cosmic-ray energies. The high sensitivity measurements at energies below 100 keV provided by this experiment will be especially critical to determining the origins of the quiet time component.

## 2.5. INTERPLANETARY SHOCKS AND THE EARTH'S BOW SHOCK

At energies of a few hundred keV to  $\sim 10$  MeV, ions are often observed to be accelerated by the passage of an interplanetary shock (see Armstrong *et al.*, 1977, for review). Enhancements of ions at even lower energies (a few keV to 40 keV) have been found on ISEE in conjunction with major interplanetary shock wave disturbances. These ions are roughly isotropic in the solar wind frame and may be solar wind ions accelerated and scattered by some mechanism associated with the shock wave disturbance (Gosling *et al.*, 1980). Similarly the Earth's bow shock accelerates ions and electrons to  $\gtrsim 10^2$  keV energies (see below).

This instrument provides high time resolution, 3D distributions over the enormous energy range of the ions and electrons which are affected by interplanetary shocks. The fast 3D measurements of ion distributions can be used to remotely sense the shock, and effectively trace particles entering and leaving the shock, and to trace the evolution of the ion distributions through the shock.

## 2.6. UPSTREAM IONS AND ELECTRONS

Ions originating at the Earth's bow shock are frequently observed in the upstream solar wind (Asbridge *et al.*, 1968; Lin, 1974). Close to the bow shock, two types of upstream ion populations have been distinguished: first, a narrow beam of ions moving outward along the interplanetary magnetic field with speeds typically several times the solar wind speed; second, a more energetic (up to 100 keV or more) component with more nearly isotropic distributions ('diffuse ions'). Paschmann *et al.* (1980) showed that the beam-like ions are simply solar wind ions reflected at the bow shock and energized by the interplanetary electric field.

The reflected ion beams may become unstable to low-frequency magnetohydrodynamic waves, in which case the beams are scattered and eventually isotropized.

The reflected ions could be the source for the lower energy diffuse ions. On the other hand the diffuse ions may be entirely unrelated, or possibly they may be accelerated between the waves produced by the reflected ions and the bow shock.

Measurements of the complete 3D ion distributions on WIND during the lunar swing-by orbit phase will provide a wealth of new information on the origin and evolution of these particle populations. Since the Wind spacecraft is expected to remain in the lunar swingby orbit for the first two years, tens of inbound and outbound crossings of the upstream foreshock region will be obtained. Furthermore, results from ISEE-3 (Anderson, 1981) show that, on occasion, the upstream particles are detected even at the L1 halo orbit distance.

Electrons of a few to  $\gtrsim 10^2$  keV are also observed far upstream from the Earth's bow shock. These particles appear to originate at the shock and their energy spectrum seems dependent on the angle between the IMF and the shock (Anderson *et al.*, 1979). These electrons may form beams which produce the electron plasma waves observed upstream (Filbert and Kellogg, 1979). Detailed 3D observations of these particles are needed to study their acceleration process, the beam plasma interaction to produce waves, and to determine their relationship to the reverse heat flow electrons at lower energies (Feldman *et al.*, 1973).

## 2.7. PARTICLE ENTRY INTO THE MAGNETOSPHERE

Some of the interplanetary ions and electrons enter the Earth's magnetosphere. There seems to be little doubt that a significant component of their entry is direct, due to IMF-magnetospheric field line connection. However, where the entry takes place and what are the physical conditions in the connection layer are not at all known. Detailed measurements of 3D particle distribution outside and inside the magnetosphere and geomagnetic tail over a very wide energy range for both ions and electrons are required. From time delays, energy spectrum comparisons and high resolution pitch angle distributions, a comprehensive picture of the entry process can be assembled. A long-term data set is required so that such a picture can be formed for a variety of interplanetary magnetic field configurations. Comparisons between wind measurements such as provided by this experiment and those obtained by similar experiments on the Geotail and Polar spacecraft over several years should be very illuminating.

## 2.8. MAGNETOSPHERIC BURSTS IN THE INTERPLANETARY MEDIUM

Occasionally bursts of ions and electrons are observed upstream from the Earth which extend to much higher energies,  $\gtrsim 0.3$  MeV, than the bow shock related particles discussed above. Based on multi-spacecraft observations of  $\gtrsim 0.2$  MeV electrons and ions, Sarris *et al.*, (1978) suggested that these particles are accelerated in the magnetosphere, and released into the interplanetary medium. The details with which such particle distributions can be measured by this Wind instrument will help establish the origin of these particles.



### 3. Instrument Overview

The basic instrument consists of three detector systems: The semi-conductor detector telescopes (SST), the electron electrostatic analyzers (EESA), and the ion electrostatic analyzers (PESA), linked together and to the spacecraft command and data handling (C&DH) system by the data processing unit (MAIN DPU). In addition there is a Fast Particle Correlator (FPC) (discussed in Section 8) for the study of interplanetary and upstream plasma wave-particle phenomena. Table I summarizes the measurement parameters and instrument characteristics. The SST consists of three arrays of semi-conductor detectors, each with a pair of double-ended telescopes to measure electron and ion fluxes above  $\sim 20$  keV. EESA-L and -H and PESA-L and -H are pairs of electrostatic analyzers with widely different geometric factors to cover the wide range of particle fluxes from  $\sim 3$  eV to 30 keV and provide significant measurements even at the lowest flux levels likely to be encountered. EESA-H is also used in the FPC and has electrostatic deflectors to follow the magnetic field.

To minimize spacecraft potential effects on low energy particles and to provide unimpeded fields of view, EESA-L and EESA-H are mounted at the end of a 0.5 m boomlet, while PESA-L, PESA-H, and the SSTs are mounted on an opposing 0.5 m boomlet (Figure 3).

To fully utilize the capabilities of these instruments, microprocessors are employed to provide physically meaningful on-board data processing and compression, as well as flexible operation. For example, ten moments of positive ion and electron distributions – density, the three components of bulk velocity, and the six unique elements of the momentum flux tensor – are computed every spin period. In addition, the particles can be sorted by pitch angle and reduced parallel distribution functions computed, using the magnetic field vector obtained directly from the on-board magnetometer. Besides the spacecraft power and C&DH interfaces, the experiment has interfaces to the magnetic field and wave experiments (see Bougeret *et al.*, 1994, and Acuna *et al.*, 1994, this volume). The wave data are used in the FPC for wave-particle correlations.

### 4. Electrostatic Analyzers (EESA and PESA)

The PESAs and EESAs have been designed for 3D measurements of the interplanetary ion and electron populations, respectively, from  $\sim 3$  eV to 30 keV. The 3D distribution of these particles will be sampled as often as every half spacecraft spin. The use of dual analyzers for both ions and electrons increases the range of fluxes that can be measured without detector saturation, allowing direct sampling of the core solar wind ion and electron populations as well as high sensitivity measurements of suprathermal plasma. The analyzer design is a symmetrical spherical section electrostatic analyzer (Carlson *et al.*, 1983) with a  $360^\circ$  or  $180^\circ$  disk-shaped

PESA/SST BOOMLET ON THE WIND SPACECRAFT  
UCB/SSL 11/91

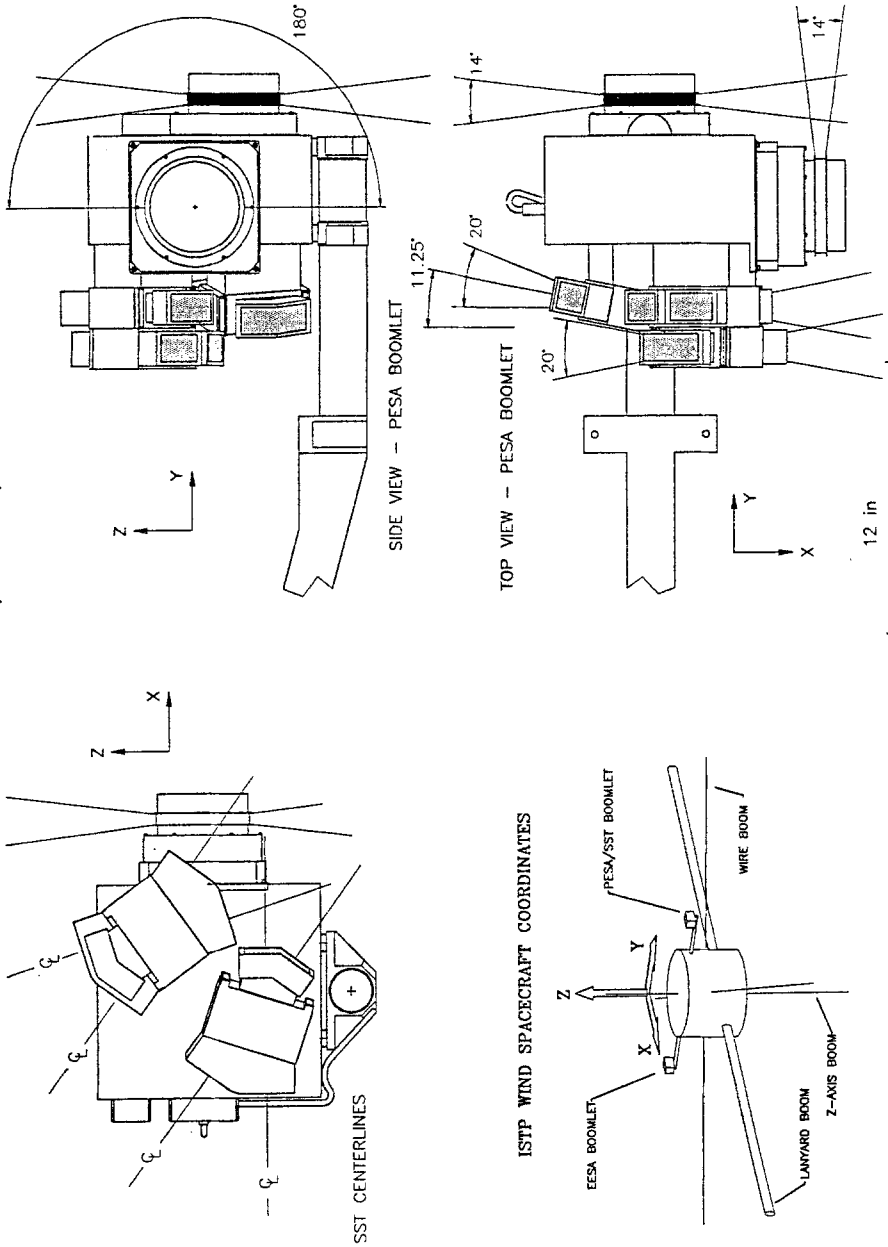


Fig. 3a. Three views of the PESA/SST boom unit, and a schematic of the boom mounting on the spacecraft (lower left).

EESA BOOMLET ON THE WIND SPACECRAFT  
UCB/SSL 11/91

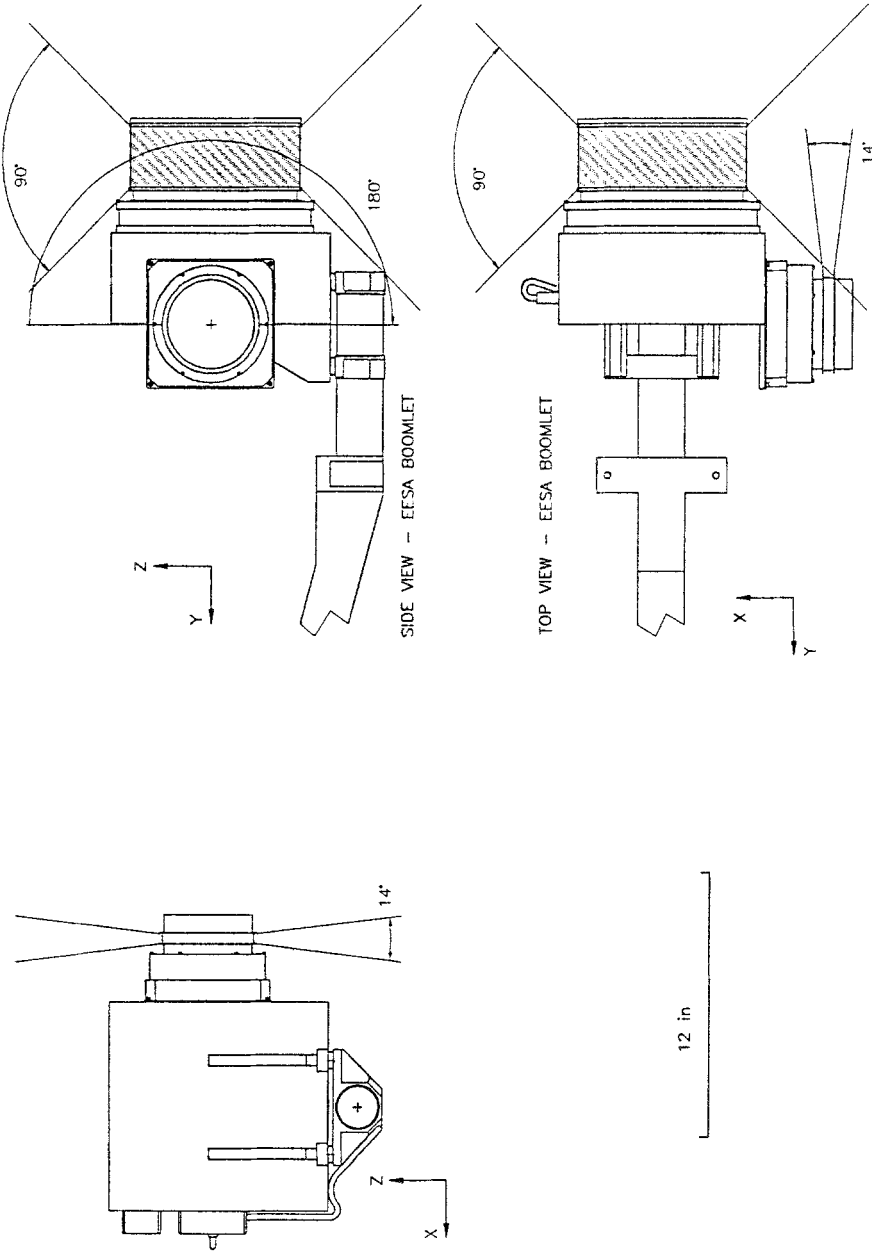


Fig. 3b. Three views of the EESA boom unit.

TABLE I  
ISTP/GGS WIND 3D plasma and energetic particles instrument

A. Measurement parameters

Detector	Particle species and energy range <sup>a</sup>	Geometric factor cm <sup>2</sup> sr <sup>f</sup>	Field of view degrees <sup>b</sup>	Dynamic range eV(cm <sup>2</sup> sr eV s) <sup>-1</sup>
EESA-H/FPC	100 eV–30 keV e	0.1 E	360 × 90 <sup>c</sup>	~1–10 <sup>8</sup>
EESA-L	3 eV–30 keV e	1.3 × 10 <sup>-2</sup> E	180 × 14	~ 10 <sup>2</sup> –10 <sup>9</sup>
PESA-H	3 eV–30 keV p	1.5 × 10 <sup>-2</sup> E	360 × 14	~10–10 <sup>9</sup>
PESA-L	3 eV–30 keV p	1.6 × 10 <sup>-4</sup> E	180 × 14	~ 10 <sup>4</sup> –10 <sup>11</sup>
SST				
Foil F	25–400 keV e	1.7 <sup>d</sup>	180 × 20 <sup>d</sup>	~0.1–10 <sup>6</sup>
Magnetic O	20 keV–6 MeV p	1.7 <sup>d</sup>	180 × 20 <sup>d</sup>	~0.1–10 <sup>6</sup>
Telescope FT	400 keV–1 MeV e	0.36 <sup>e</sup>	72 × 20 <sup>e</sup>	~ 10 <sup>-2</sup> –10 <sup>6</sup>
OT	6–11 MeV p	0.36 <sup>e</sup>	72 × 20 <sup>e</sup>	~ 10 <sup>-2</sup> –10 <sup>6</sup>

B. Instrument characteristics

	Mass kg	Power watts	Volume cm	Bit rate
EESA-H and EESA-L Boom Unit	5.2	3.2	31 × 35 × 25 <sup>g</sup>	
PESA-H, PESA-L, and SST boom unit	5.6	4.0	33 × 27 × 25 <sup>g</sup>	
Main DPU/SST analog box	7.4	8.4	20 × 20 × 26	
Total	18.2	15.6		1035 bps <sup>h</sup>

<sup>a</sup> Energy resolution  $\Delta E/E$  is ~ 0.2 for EESAs and PESAs and ~0.3 for SSTs.

<sup>b</sup> For EESAs and PESAs the angular resolution is 5.6° resolution within ±22.5° from ecliptic plane, 11.25° resolution to ±45°, then 22.5° resolution beyond. For SSTs the resolution is 22.5° × 36°.

<sup>c</sup> 14° FOV electrostatically deflected up to ±45° to follow magnetic field.

<sup>d</sup> Five detectors cover the 180° FOV, with geometric 0.33 cm<sup>2</sup> sr each.

<sup>e</sup> Two telescopes cover the 72° FOV, with geometric factors 0.33 and 0.03 cm<sup>2</sup> sr (telescope 2 has reduced geometric factor).

<sup>f</sup>  $E$  is usually in eV.

<sup>g</sup> Approximate outside dimensions.

<sup>h</sup> Bit rate doubles inside 60  $R_E$ .

field of view (Figure 4). The imaging of parallel rays onto the detector plane provides about 1° inherent analyzer resolution (Figure 5). The analyzer geometry forces at least a 2 bounce light path, and the smooth inner and scalloped outer hemispheres have a gold black coating applied to further reduce scattered light. A very similar analyzer has been flown on the Mars Observer spacecraft and has provided good solar UV rejection. A grid at the analyzer exit eliminates leakage

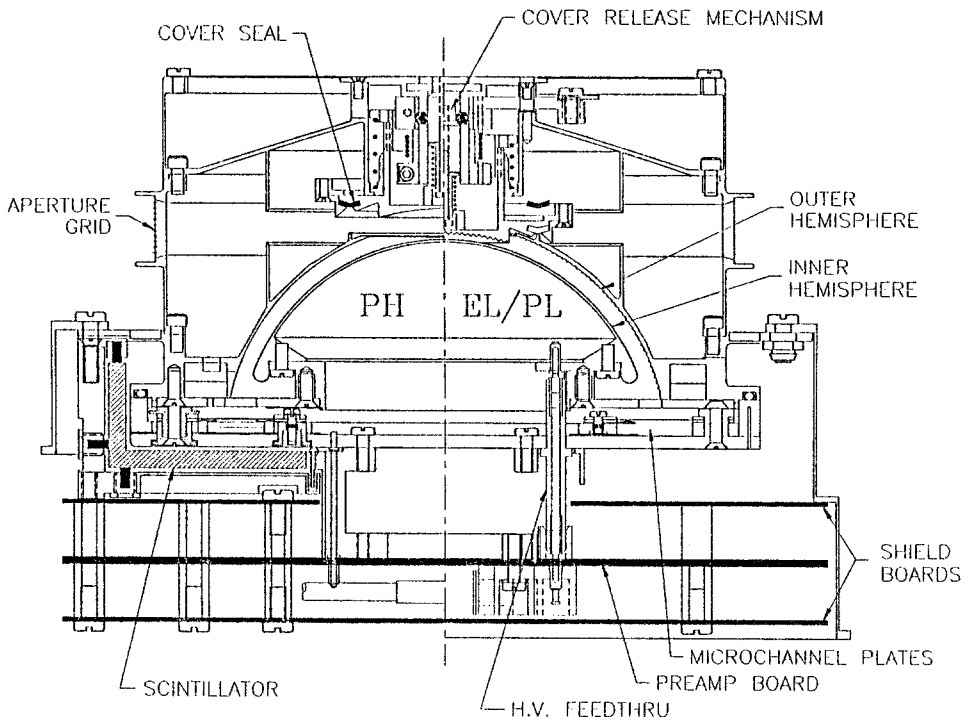


Fig. 4. Cross section of an electrostatic analyzer representative of PESA-H (*left side*), and PESA-L and EESA-L (*right side*).

field from the microchannel plates (MCPs) from entering the analyzer section. The inside of the analyzer is sealed by an aperture cover, together with a one-time opening mechanism, which maintains an internal dry nitrogen environment during integration and launch.

PESA-H and PESA-L have identical electrostatic deflection systems with inner hemisphere radius of 3.75 cm, plate separation of 0.28 cm, top-cap separation of 0.56 cm, and entrance opening half angle of  $19^\circ$ . This gives a  $\Delta E/E = 0.20$  FWHM and angular acceptance of  $\pm 7^\circ$  (7.5° FWHM). Figure 6 shows the analyzer's energy and angle response. Ions are post-accelerated by a  $-2500$  V potential applied between the front of the MCP and a grid located 1 mm above the MCPs to increase ion detection efficiency. PESA-H has a  $360^\circ$  field of view (FOV) tangent to the spacecraft surface. Penetrating particle background is rejected from PESA-H (and EESA-H) by an L-shaped plastic anticoincidence scintillator that surrounds the MCPs (Figure 4). MCP pulses coincident with light pulses in the scintillator are rejected. With an analyzer geometric factor of  $0.04E$  cm<sup>2</sup>-sr (determined by computer simulation) where  $E$  is the particle energy (usually in eV), a microchannel plate (MCP) detector efficiency of about 50%, and a grid entrance post transmission of 75%, the PESA-H total geometric factor (summed over all anode sectors) is about  $0.015E$  cm<sup>2</sup>-sr.



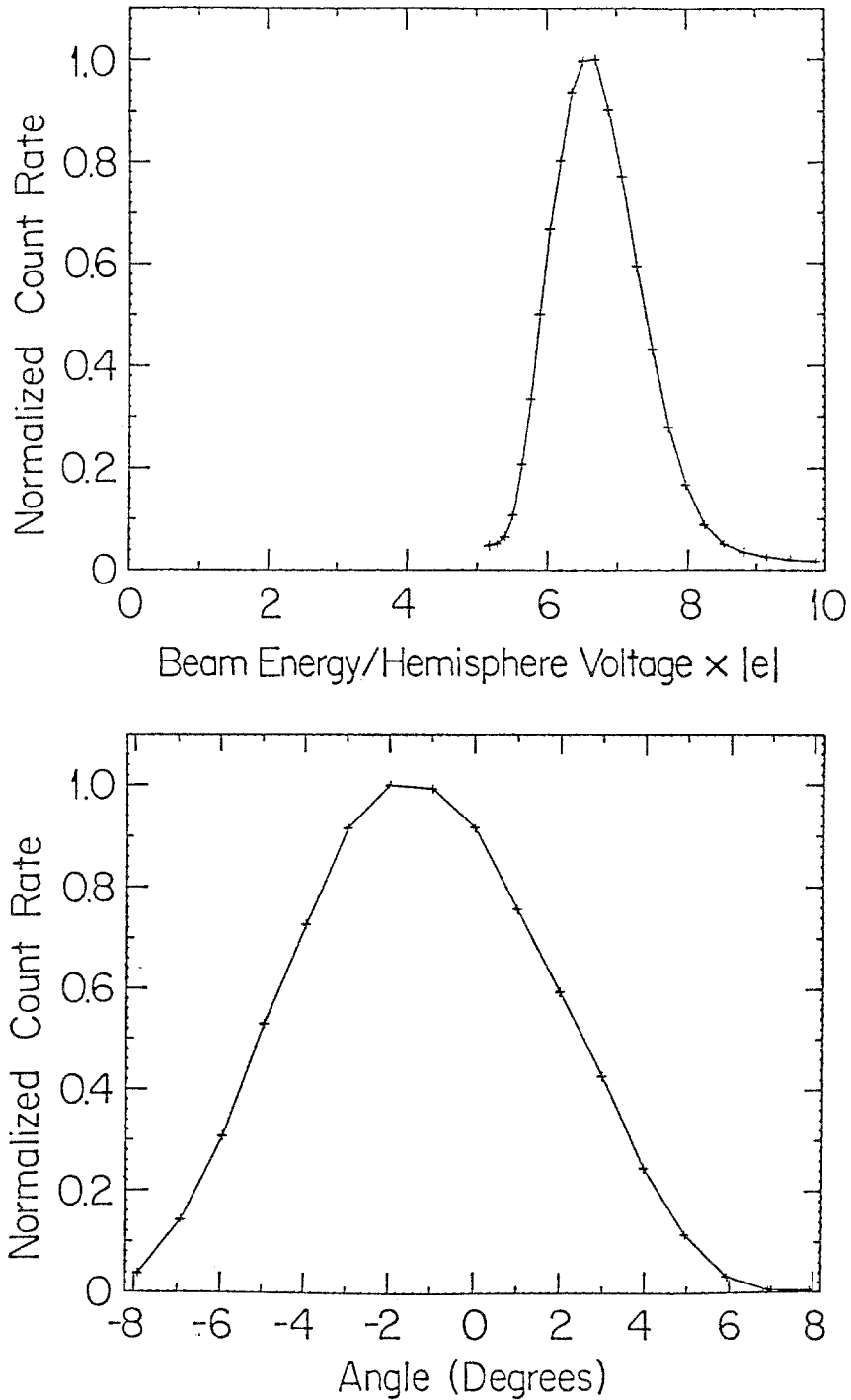


Fig. 6. Typical calibration curves for the electrostatic analyzer energy response (*top*) and angular response (*bottom*). The zero of the angle scale is arbitrary.

PESA-L has a  $180^\circ$  FOV radial to the spacecraft and does not have an anticoincidence scintillator (Figure 4, right side). The response of PESA-L is attenuated by a factor of 50 by the collimator/attenuator with uniformly spaced 0.24 mm diameter holes with  $1 \text{ mm} \times 2.25 \text{ mm}$  spacing. This produces an analyzer with identical energy-angle response as the PESA-H but with a total geometric factor of only  $1.6 \times 10^{-4} E \text{ cm}^2\text{-sr}$ .

The EESA-L analyzer is nearly identical to the PESA-L with a  $180^\circ$  FOV radial to the spacecraft and no anticoincidence scintillator. Electrons are post-accelerated by a +500 V potential applied to the front of the MCP to increase detection efficiency to about 70%. A single grid attenuation gives the EESA-L a total geometric factor of  $1.3 \times 10^{-2} E \text{ cm}^2\text{-sr}$ .

EESA-H has a  $360^\circ$  planar FOV that is tangent to the spacecraft surface. The EESA-H FOV can be electrostatically deflected into a cone up to  $\pm 45^\circ$  out of its normal plane by voltage applied to curved plates placed at the analyzer entrance aperture (Figure 7). Leakage fields from the deflectors are minimized by a pair of grids at the outer analyzer collimator. The deflectors allow the analyzer FOV to follow the magnetic field as the spacecraft spins. This mode will be used primarily to increase the measurement time of field aligned electrons during times of strong wave activity, such as during type III radio bursts, for the Fast Particle Correlator experiment (see Section 8).

The EESA-H analyzer has an inner hemisphere with radius of 8.0 cm, plate separation of 0.6 cm, top-cap separation of 1.2 cm, and entrance opening half angle of  $19^\circ$ . The EESA-H has the same  $\Delta R/R$  and opening angle as the EESA-L and the PESAs, resulting in the same energy and angle response as shown in Figure 6. The EESA-H total geometric factor calculated from the analyzer geometric factor of  $0.20 E \text{ cm}^2\text{-sr}$ , MCP efficiency of about 70% and grid transmission (3 grids), of 73%, is about  $0.1 E \text{ cm}^2\text{-sr}$ .

All the EESAs and PESAs use MCP detectors in a chevron pair configuration which gives an electron multiplication gain of about  $2 \times 10^6$  and a narrow pulse height distribution. The MCPs are each 1 mm thick and have a bias angle of  $8^\circ$ . A single  $180^\circ$  half ring chevron pair is used in the PESA-L and EESA-L analyzers. Two sets of half rings are used in the PESA-H sensor to form a  $360^\circ$  ring. The EESA-H uses six  $60^\circ$  sector MCPs to form a  $360^\circ$  ring. This configuration minimizes variations in detection efficiency due to changes in the angle between the microchannel bias angle and particle incident angle on the MCP. The plates are processed for high strip current to provide fast counting capability.

Charge pulses produced by the MCPs are collected on a set of discrete anodes and sent to pre-amplifier-discriminators (AMPTEK A111) and accumulated into 24-bit counters (8C24) mounted on the amplifier board. The pre-amplifiers can be tested in flight by a pulse generator that feeds a set of input capacitors at the front of the pre-amplifier circuit. The pre-amplifier board also contains a circuit to allow the determination of MCP pulse height distributions.



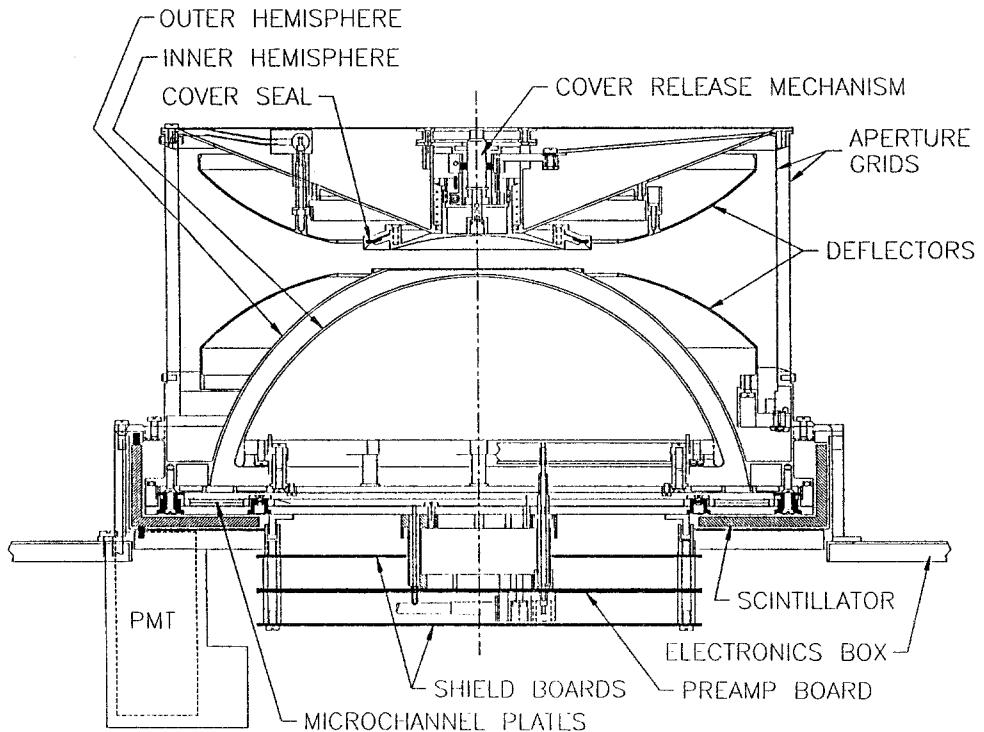


Fig. 7. Cross section of the EESA-H analyzer, showing the electrostatic deflectors.

The MCP pulses are collected by anodes etched onto a multilayer polyimide circuit board that forms the base of the analyzer-microchannel plate housing. The high (-H) and low (-L) sensitivity analyzers contain 24 and 16 discrete anodes respectively (Figure 8). The anode layout provides a  $5.6^\circ$  angular resolution within  $\pm 22.5^\circ$  of the ecliptic plane, widening to  $22.5^\circ$  normal to the ecliptic plane.

The analyzers are swept logarithmically in energy and the counters are sampled 1024 times per spacecraft spin ( $\sim 3$  ms sampling period). The analyzer can be programmed with 64 energy samples per sweep and 16 sweeps per spacecraft spin, or 32 energy samples and 32 sweeps, etc. A representative operating mode when the spacecraft is in the solar wind may have:

- (1) EESA-L measuring the solar wind core and halo electrons with a 32 sample energy sweep from 3 eV to 300 eV, 32 times a spin. With  $11.25^\circ$  spin phase resolution, there will be no gaps in EESA-L's sampling in the ecliptic plane.

- (2) EESA-H measuring the distribution of electrons associated with type III radio bursts with a 32 sample energy sweep from 300 eV to 30 keV, each  $11.25^\circ$  of spacecraft spin.

- (3) PESA-L measuring solar wind ions and ion beams reflected at shocks with a 16 sample energy sweep from 100 eV to 10 keV, each  $5.6^\circ$  of spacecraft spin.

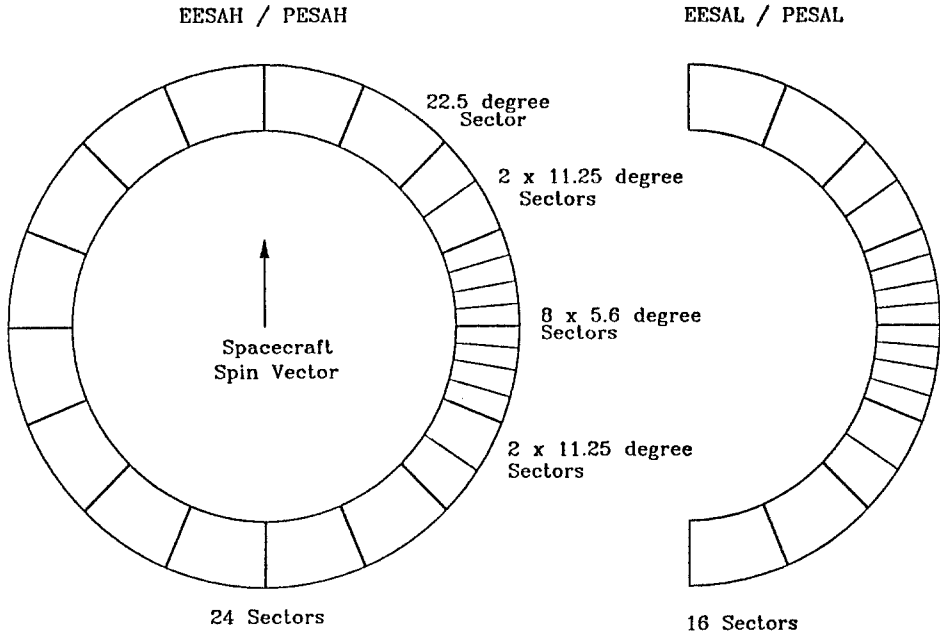


Fig. 8. The pattern of discrete anodes for the high (-H) sensitivity and low (-L) sensitivity electrostatic analyzers.

(4) PESA-H measuring the suprathermal ion spectra with a 32 sample energy sweep from 3 eV to 30 keV, each  $11.25^\circ$  of spacecraft spin.

### 5. Semi-Conductor Detector Telescopes (SST)

Three arrays, each consisting of a pair of double-ended semi-conductor detector telescopes (Figure 9), provide high sensitivity, high energy resolution, three-dimensional measurements of  $>20$  keV electrons and ions. Each telescope consists of either a pair or triplet of closely-sandwiched semi-conductor detectors. The center detector (T) of the triplet is  $1.5 \text{ cm}^2$  in area, 500 microns thick, while all other detectors are  $1.5 \text{ cm}^2$  area, 300 microns thick. Each sandwich of detectors is arranged in a double-ended telescope. In one direction the detector is covered with a thin lexan foil whose thickness is chosen to stop protons of energy up to the energy of electrons ( $\sim 400$  keV) which penetrate the 300 micron detector. The foil leaves the electron spectrum essentially unchanged. In the opposite direction, the two telescopes of an array look through a common broom magnet, which sweeps away electrons below 400 keV, but leaves ions unaffected. In the absence of higher energy particles, the foil (F) detectors count only electrons while the magnet or open (O) detectors measure only ions. To achieve low background, the output of each detector is taken in anti-coincidence with the detector behind it. The very

SOLID STATE TELESCOPE  
UCB/SSL  
JULY 91

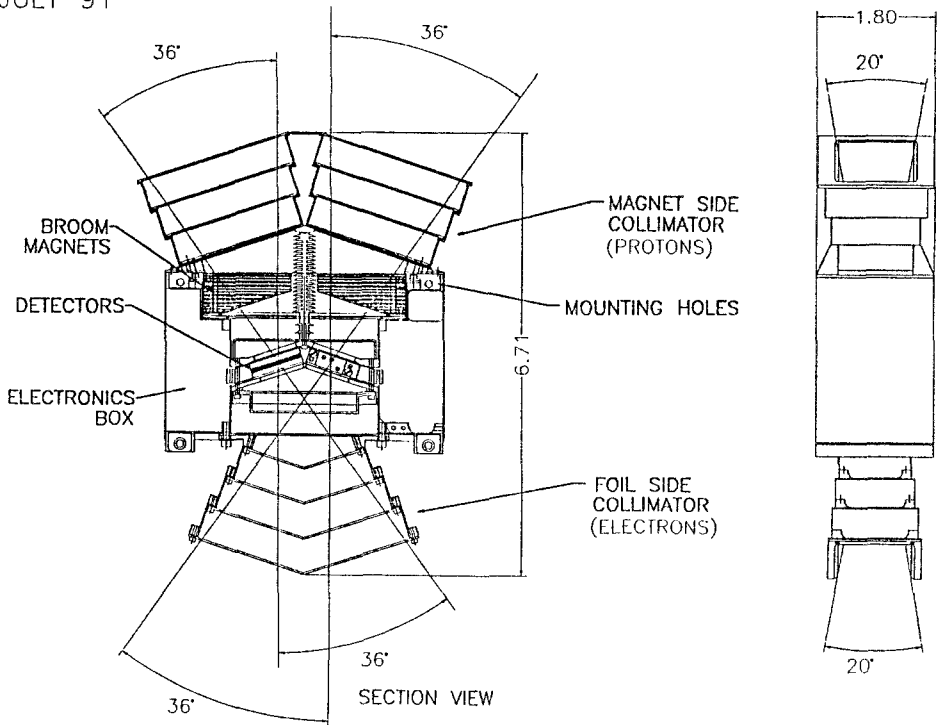


Fig. 9. An array of two double-ended telescopes is shown in a section view. Particles entering the two upper collimators pass through a sweep magnet while those entering the lower collimator pass through a thin lexan foil.

close spacing ( $\lesssim 10^2$  microns) between detectors essentially eliminates counts from penetrating particles.

Most  $>400$  keV electrons penetrate the front detectors and are rejected by the anticoincidence with the adjacent detector, although because of straggling some  $>400$  keV electrons will stop in the front detectors. Electrons from  $\sim 400$  keV to  $>1$  MeV are cleanly measured by the sum of the front and center detector outputs of the triplet (FT or OT) when they are in coincidence. Protons up to  $\sim 6$  MeV stop in the front detectors, and  $\sim 6$ -11 MeV protons are detected by the combination of the front and center (OT) detectors in the triplet.

Each double-ended telescope has two  $36^\circ \times 20^\circ$  FWHM fields of view so five telescopes cover a  $180^\circ \times 20^\circ$  slice for magnet detectors and an analogous slice for foil detectors (Figure 10). As the spacecraft rotates through  $360^\circ$  each slice sweeps out the full  $4\pi$  steradians. Telescope 6 views the same angle to the spin axis as telescope 2. Both ends of telescope 2 are equipped with a drilled tantalum cover to reduce the geometric factor by a factor of ten to accommodate the most

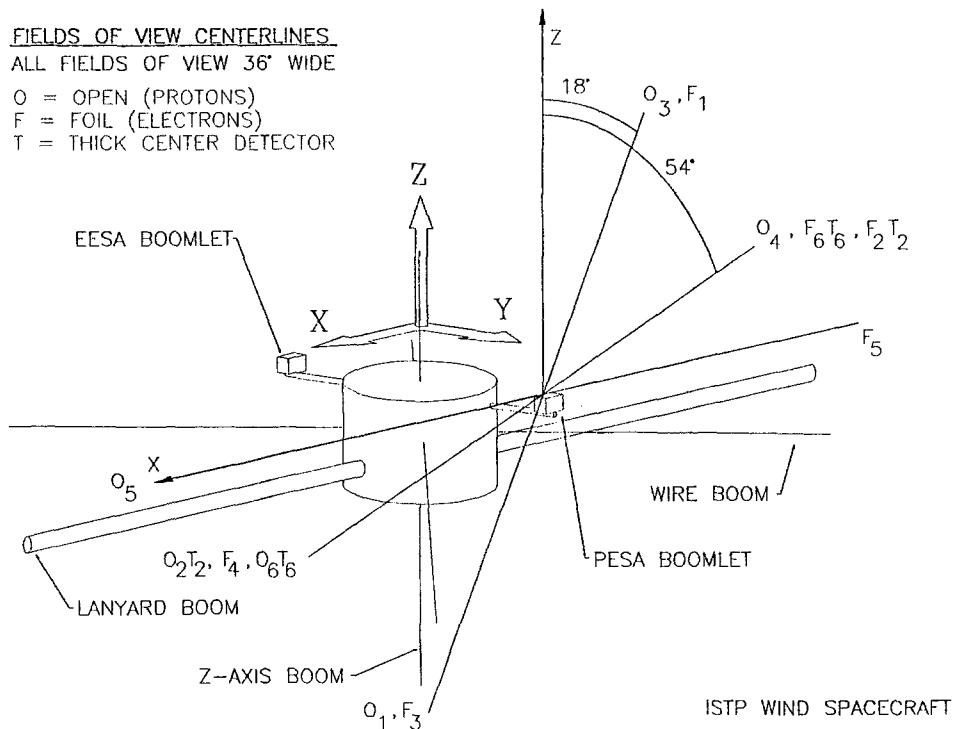


Fig. 10. Schematic indicating the centers of the FWHM fields of view for the SSTs relative to the spacecraft spin axis. Telescope 2 ( $F_2T_2$  and  $O_2T_2$ ) is covered by a drilled tantalum cover to reduce its geometric factor.

intense fluxes. The field of view of the triplet telescopes 2 and 6 cover 36° to 72° and 108° to 144° to the spin axis.

The foils over the electron detectors have 1500 Å of aluminum evaporated on each side to completely eliminate sunlight. The collimator keeps sunlight from directly impinging on any detector except  $O_5$ , and the inside of the collimators is blackened to reduce scattered light to below the threshold of the detectors. The electronics are designed for fast (approx. 130 ms) recovery from the current pulse produced in  $O_5$  when it views the Sun. Thus only ~30 deg of rotation of detector  $O_5$  is lost due to sunlight. During this time the output from  $O_5$  is blocked from entering the analog to digital converter (ADC).

The fully depleted, passivated ion-implanted silicon detectors used in these telescopes have exceptionally low leakage currents,  $\lesssim 10$  nA at room temperature. The SSTs are thermally isolated from the spacecraft to achieve temperatures of  $\sim 0^\circ$  C and reduce detector thermal noise to negligible levels.

Figure 11 shows a block diagram of the SST analog electronics. The outputs from each detector are fed to low-noise charge-sensitive pre-amplifiers which are mounted next to the detectors, and then to shaping amplifiers. The shaped pulses are multiplexed into linear ADCs. The outputs of the ADCs are pseudo-log compressed

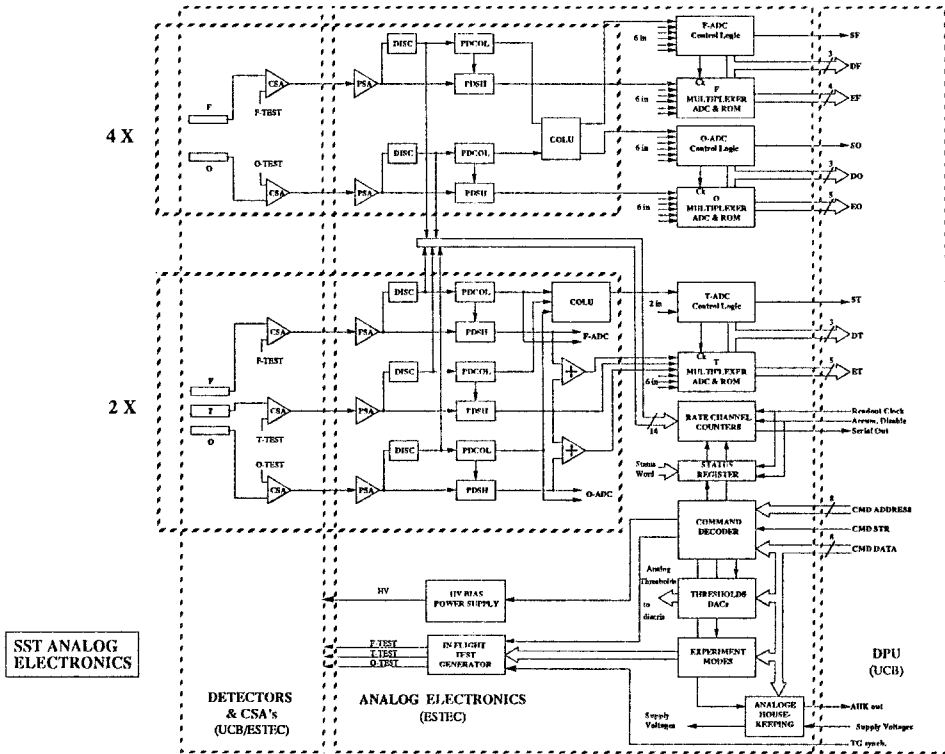


Fig. 11. Block diagram of the SST analog electronics.

to 24 energy channels for all O, OT, and FT outputs, and 16 energy channels for the F outputs, with  $\Delta E/E$  of about 30% over the range of energies.

The SSTs are calibrated in flight by various combinations of three linear ramp pulsers, one each for the F, O, and T detectors, operating at 500 Hz and fed into the pre-amp inputs. Absolute energy calibration points are obtained by monitoring the highest energy of protons which stop in the detectors, and by placing the pairs or triplets of detectors in coincidence and monitoring the minimum ionizing energy for penetrating particles. Both of these energies depend only on the thickness of the detector.

## 6. Digital Electronics

The digital electronics consists of three micro-processor systems, together with associated control and data collection circuitry, as shown in Figure 12. Each processor is dedicated to a specific set of tasks, and is attached to the appropriate interfaces to carry out these tasks. All processors are remotely programmable to a large extent, allowing a great deal of flexibility for detector operation and telemetry allocation. Only the main processor, the low voltage power supply, and the interface

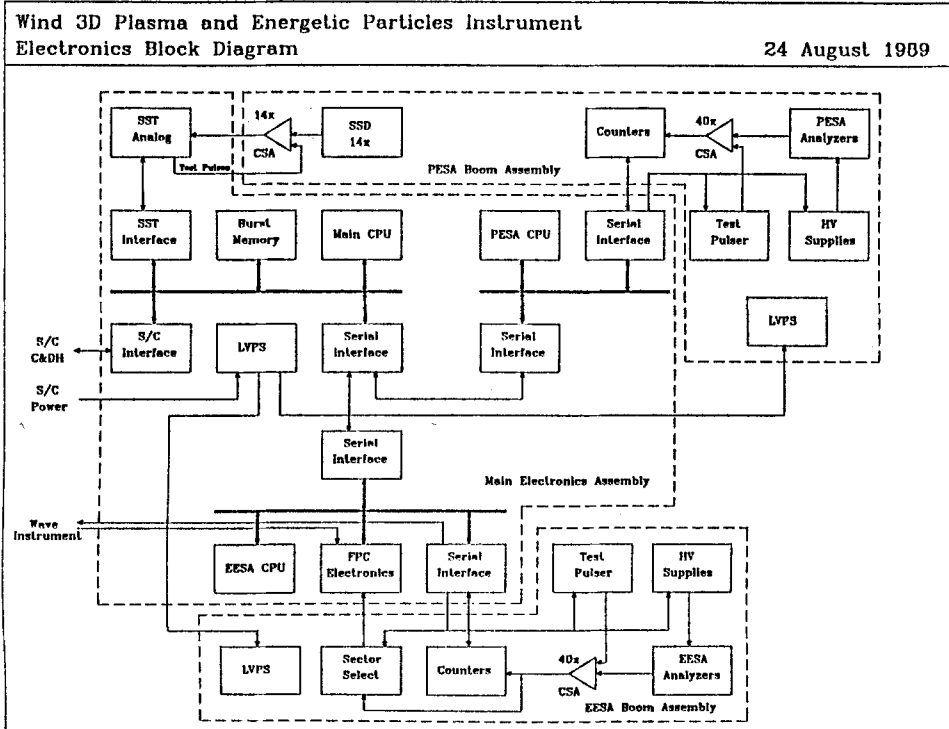


Fig. 12. Block diagram of the instrument electronics.

to the spacecraft are crucial to the operation of the entire experiment; other systems are isolated so that a failure in one only affects that part of the experiment.

The main processor is primarily responsible for interfacing to the spacecraft C&DH system through a spacecraft interface. It selects data from the three detector systems via a programmed telemetry collection cycle and formats it into the telemetry channel. Incoming commands are executed and/or passed on to the other processors. The main processor has a large (2 megabyte) burst memory to store data at high rate during selected events, to be played back at lower rate in the normal telemetry. The main processor also serves as the SST processor, controlling the SSTs and collecting and formatting their data.

Separate EESA and PESA processors control the EESAs and PESAs and collect and compress their data. These processors interface with the EESA and PESA controls and counters via serial interfaces to the boom units. The compressed data is passed through a second serial interface to the main processor; since the data is compressed, the transfer rate is a small fraction of the EESA and PESA data collection rate. In addition, burst data come through this interface. The EESA processor also supports the FPC.

This organization of tasks among the various processors is simple and powerful. The different analyzers are controlled independently, so the data collection mode

of one analyzer may be changed without affecting the other analyzers. The main electronics box is mounted on the spacecraft body. It includes all three processors, and the analog electronics for the SSTs.

## 7. Experiment Modes of Operation

The instrument modes are highly programmable via instrument control and telemetry selection tables, and by program up-link. The default, or 'Solar Wind' instrument mode, which the instrument runs on power-up, is suitable for nominal solar wind operations. Other modes are variations on this mode, with emphasis on different measurements. The instrument automatically adjusts to different telemetry rates by changing the number of spins averaged over for each data product in the telemetry.

The SSTs collect data 16 times per spin in 16 energy channels for F and 24 channels for O, OT, and FT detectors, for each of 6 F detectors, 6 O detectors, 2 FT, and 2 OT coincidence sums. These data are used to generate a number of telemetry products. Spectra are generated from each detector with the highest energy resolution. Full three-dimensional distributions with 40 roughly equal solid angle samples and reduced energy resolution (7 channels for F and FT detectors, and 9 for O and OT detectors) are also computed. The time resolution of 3-D distribution data varies with energy band; the lower energy bands are read out more often than the higher energy bands. Electron data is also available as Pitch Angle Distributions (PAD), by re-binning the two-dimensional angular phase space into a one-dimensional phase space based on the magnetic field direction provided by the magnetometer. The PADs are smaller than 3-D distributions, and so can be transmitted more often.

PESA and EESA analyzers are swept over their energy range 32 or 64 times per spin, as described above. Data is collected 1024 times per spin for each of 80 anodes (16 for EESA-L, 24 for EESA-H, 16 for PESA-L, and 24 for PESA-H). Telemetry products computed from this data include moments (density, velocity, pressure tensor, and heat flux), full three-dimensional distributions with various angular and energy resolutions, and snapshots of a small subset of the distribution with high angular resolution to capture beams, such as the solar wind. PADs can also be calculated from the EESA data similar to those for the SST F detectors described above. A snap-shot of the parallel distribution function may also be computed from the EESA data.

The FPC generates data in the manner described in Section 8. When no data is available from the FPC, its telemetry is automatically re-allocated to the other sensors.

The main processor is equipped with a 2 megabyte burst memory, which is used for high speed data capture during 'events'. A number of event triggers, based on the measured data, are monitored by the processor. When an event is triggered, data

from each of the analyzers is stored into the burst memory with maximum time resolution. Burst data usually consists of moderate resolution three-dimensional distribution functions. The instruments provide a constant stream of this burst data so that pre-trigger data can be stored. Data collection continues until the event ends or the buffer is filled. The data is then telemetered down using a fraction of the normal telemetry bandwidth. The burst memory is usually configured as two buffers. The system is designed to keep the ‘best’ event captured during the time it takes to telemeter the previous event.

## 8. Fast Particle Correlator

The Fast Particle Correlator (FPC) uses a direct wave-particle correlation technique and two auto-correlation techniques to examine particle bunching. A major goal of the FPC is to measure the perturbation to the electron distribution function in large amplitude Langmuir waves upstream of the Earth’s bow shock and during solar type III radio bursts. The FPC was also designed to study other wave-particle interactions in the interplanetary medium, interplanetary shock, the bow shock, and in the magnetosphere.

The FPC performs three types of correlations: direct wave-particle correlations, auto-correlations, and burst correlations. The EESA-H electron detector used by the FPC has electrostatic deflectors to provide up to  $\pm 45^\circ$  deflection, so the EESA-H field of view can include the magnetic field for one-half the time if the magnetic field is in the ecliptic. If the magnetic field is more than  $45^\circ$  from the ecliptic plane, the analyzers field of view can include the magnetic field continuously. The EESA-H can be directed to measure a narrow energy range that includes a region where the parallel distribution function has a positive slope ( $df_{\parallel}/dv_{\parallel} > 0$ ), if such a region exists. In this way the FPC can study an electron beam and correlations with high time resolution. Finally, the EESA-H has a large geometric factor, necessary to obtain statistically significant results.

The direct wave-particle correlator and the burst correlator provide a much higher data rate than can be telemetered so they must be operated with a limited duty cycle. To optimize the quality of the data, they are only operated if the wave electric field signals are strong enough that we can expect significant fluctuations to the electron distribution. The trigger level is selectable.

### 8.1. DIRECT WAVE-PARTICLE CORRELATION

The direct wave-particle correlation essentially approximates a correlation function between the electron flux and the electric field signal:

$$C(v, \Theta) = \frac{\int E_0 \sin(kx - \omega t + \Theta) F(v, t) dt}{\langle E^2(t) \rangle_t^{1/2} \langle F^2(v, t) \rangle_t^{1/2}},$$



where  $E = E_0 \sin(kx - \omega t)$  is the wave electric field,  $F(v, t)$  represents the electron flux,  $\Theta$  is the instrumental phase shift, and  $\langle \rangle_t$  indicates a time average. A second correlation  $C(v, \Theta + \pi/2)$  can be combined to determine the amplitude, relative phase, and electron velocity of a perturbation to the electron distribution at the incident wave frequency.

The direct wave-particle correlator, diagramed in Figure 13, is similar to an instrument flown on an auroral sounding rocket (Ergun *et al.*, 1991). The raw, wide-band electric field signal ( $E_x$  or  $E_y$ ) is obtained from the WAVE experiment. There are two orthogonal electric field antennae normal to the spin axis and the antenna that lies closest to parallel with the ambient magnetic field is chosen. The signal is fed to one of four high pass filters and one of four low pass filters. It is also possible to bypass either one or both sets of filters. The Langmuir emissions generally have frequencies between 12 and 50 kHz, so the filters were designed to isolate this frequency band.

The conditioned electric field signal is fed to a broad band rectifier and an analog phase splitter. The broad band rectifier supplies the amplitude of the wave signal to the microprocessor for triggering. The analog phase splitter consists of two active all-pass filter networks which provide phase shifts that differ by  $90^\circ \pm 3^\circ$  over a 5 to 125 kHz frequency range. The outputs of the phase splitter, designated the SIN phase ( $\Theta + 0^\circ$ ) and the COS phase ( $\Theta + 90^\circ$ ), each undergo an amplification of ten and are digitized by a comparator to one bit which represents the polarity of the wave signal. A baseline restorer system is incorporated to eliminate false correlations from a dc bias or asymmetric signal. The baseline restorer is a differential integrator which controls the dc level of the comparators negative input. This system maintains a  $(50.0 \pm 1.0)\%$  duty cycle over a 1 s period.

The WIND FPC incorporates a digital calibration system to monitor the duty cycles of the digitized wave signals continuously. The digitized wave signal and the particle events are synchronized to a fixed 5 MHz clock, allowing the duty cycle to be timed to  $\pm 100$  ns over the  $\sim 3$  ms integration period.

Particle counts from EESA-H increment three counters which are designated the total count, SIN count, and COS count. The SIN (or COS) counter is incremented only if the polarity of the SIN (or COS) wave signal is positive. A microprocessor subtracts the total count from twice the contents of the SIN (and COS) counter and renormalizes the data using the duty cycle measurement. The two  $90^\circ$  phase shifted data sets are designated the SIN correlation and the COS correlation. Separate correlation measurements are made for up to four channels of the EESA-H.

The amplitude and phase of the electron bunching can be determined by combining the SIN correlation and COS correlation results. If we assume the electron bunching is sinusoidal, the amplitude of the correlation is the square root of the sum of the squares of the SIN and COS correlations. The phase is the negative of the inverse tangent.

Instrumental phase shifts and time delays must be carefully calibrated. The largest phase shift comes between the electric field antennae and the counter gates

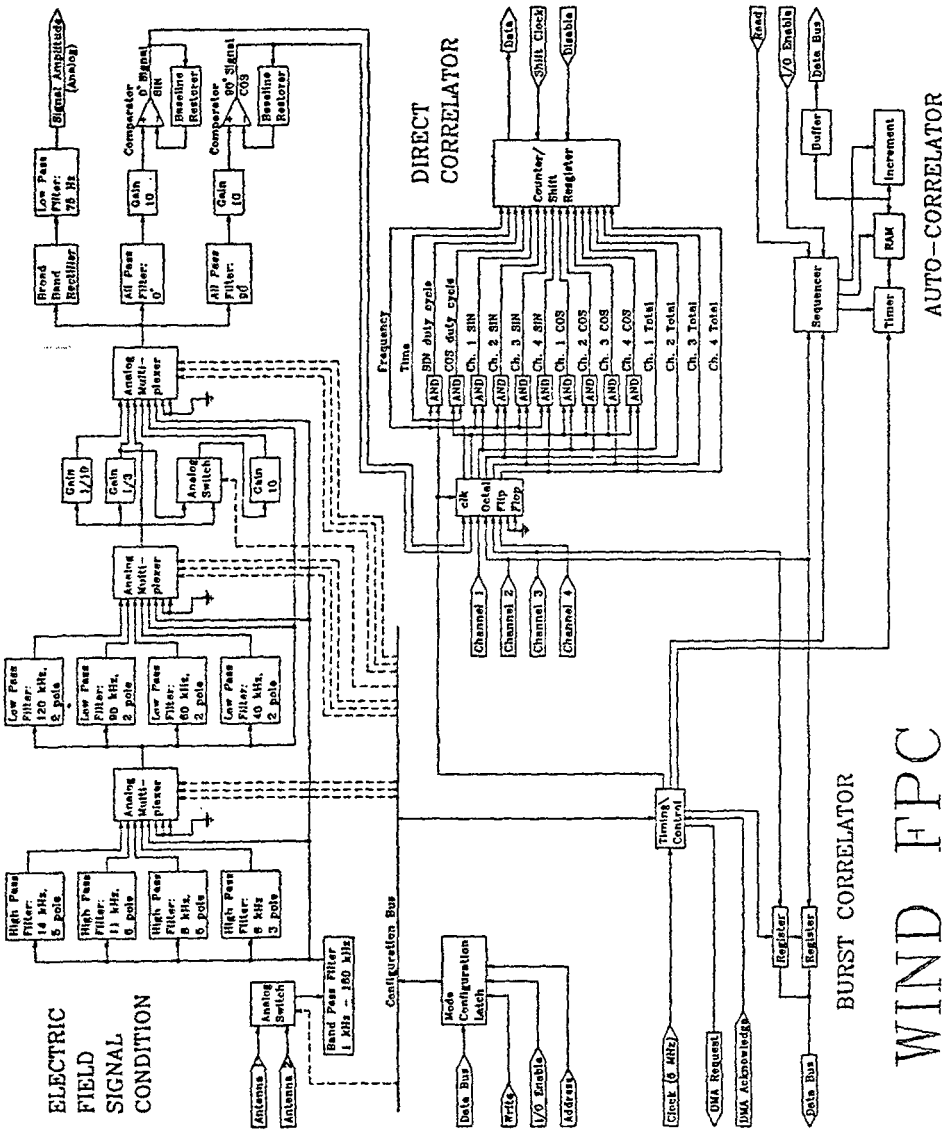


Fig. 13. Block diagram of the FPC electronics.

on the wave particle correlator. This frequency dependent phase shift includes the sensor pre-amplifiers, the differential amplifiers, the band pass filters, the analog phase splitter, the comparators, the digital synchronization, and any time delay in propagation between the electric field instrument and the FPC. Other phase shifts are from the time delays in the EESA-H pre-amplifiers and the relative physical positions of the wave antennae and the EESA-H. We expect to calibrate the total phase instrumental phase shift as a function of frequency to  $\pm 10^\circ$ .

## 8.2. AUTO-CORRELATION AND BURST CORRELATION

Auto-correlation techniques do not record phase information. Although phase information can be extremely valuable, direct correlations can be diluted if the incident waves do not remain coherent over the integration period. Particle auto-correlation techniques, however, can be more sensitive to long period correlations, particularly gyroresonant bunching.

The WIND FPC auto-correlator (Figure 13) implements a technique similar to that used by Gough (1985). Histograms of the time intervals between electron counts are compiled over  $\sim 1$  s to  $\sim 2$  min periods. A particle event from the EESA-H analyzer starts a counter that is clocked by a fixed 625 kHz signal. The next particle event stops the clock. A random-access memory (RAM) is incremented at the address that the counter holds, which corresponds to the time between the electron events. A deviation of this auto-correlation histogram from the expected Poisson distribution indicates electron bunching at a frequency that is the inverse of the bunching period.

For the burst-correlation, a 625 kHz stream is modulated with the particle events. A high signal indicates that one or more particles have arrived in the  $1.6 \mu\text{s}$  period. A low signal indicates no electron events. The data is recorded periodically in 1024-bit continuous bursts. The WIND instrument stores the bursts in a 512 Kbyte section of a 2-Mbyte memory. Only  $\sim 3$  s of data from two electron channels can be stored.

The burst correlator data is analyzed by Fourier transforming the continuous bursts. A number of spectra may be averaged to increase the sensitivity. The burst correlator and direct correlator techniques should be more sensitive to small amplitude perturbations than the auto-correlator. The sensitivity of the auto-correlator is reduced by the ratio of its minimum bandwidth to its maximum bandwidth.

## 8.3. STATISTICAL UNCERTAINTIES

Detecting a perturbation to the electron distribution of 1% requires 90 000 counts in one energy bin to obtain a  $3\sigma$  ( $\sigma = \sqrt{N}$ ) confidence level. Since Langmuir waves upstream of the bow shock and in solar type III radio bursts appear in bursts of a few hundred ms, count rates of up to  $\sim 1$  MHz are required to obtain statistically significant measurements of 1% perturbation. The EESA-H analyzer used by the

FPC combines increased physical size (16 cm diameter) with increased velocity acceptance width to maximize the count rate.

## 9. Summary

This instrument is designed to provide significant measurements of the plasma environment of the near-earth interplanetary medium over a very wide range of energies, angles, fluxes, and temporal resolutions. Because of the enormous amount of data generated and the limited downlink data rate, very substantial data selection and compression are required. Furthermore, the burst memory and Fast Particle Correlator provide additional flexibility to address specific scientific phenomena. Thus, it is anticipated that instrument operation will involve significant learning and interactive reprogramming during the life of the mission to optimize the scientific return. On a routine basis, however, this experiment will provide measurements of solar wind ion velocity, temperature, and density; solar wind electron velocity, temperature, and density; as well as suprathermal ion and electron fluxes in four energy bands as key parameters directly to the GGS community.

## Acknowledgements

The efforts of R. Campbell, J. Lambert, S. McBride, J. H. Primbsch, R. Sterling, P. Turin, and R. Wilkes at UCB are gratefully acknowledged. CESR acknowledges the support on the design and manufacturing of the digital electronics by J. Rouzaud and P. Souleille. The program at CESR was supported by CNES contracts. SSD acknowledges the support on the design and manufacturing of the SST analogue electronics by T. Beaufort, J. M. Bouman, R. Brough, B. Christensen, J. Heida, L. C. Smit, and R. Scheper. The program at UCB was supported by NASA Contract NAS 5-30366, and at UW by NAS5-26850.

## References

- Acuna, M. *et al.*: 1993, this volume.
- Anderson, K. A.: 1981, *J. Geophys. Res.* **86**, 4445.
- Anderson, D. A., Lin, R. P., and Potter, D. W.: 1982, *Space Sci. Rev.* **32**, 169.
- Anderson, K. A., Lin, R. P., Martel, F., Lin, C. S., Parks, G. K., and Rème, H.: 1979, *Geophys. Res. Letters* **6**, 401.
- Armstrong, T. P., Chen, G., Sarris, E. T., and Krimigis, S.M.: 1977, in M. A. Shea *et al.* *Study of Travelling Interplanetary Phenomena*, D. Reidel Publ. Co., Dordrecht, Holland, p. 367.
- Asbridge, J. R., Bame, S. J., and Strong, I. B.: 1968, *J. Geophys. Res.* **73**, 5777.
- Barnes, C. W. and Simpson, J. A.: 1976, *Astrophys. J.* **210**, 191.
- Bougeret, J.-L.: 1993, this volume.
- Carlson, C. W., Curtis, D. W., Paschmann, G., and Michael, W.: 1983, *Adv. Space Res.* **2**(7), 67.
- Ergun, R. E., Carlson, C. W., McFadden, J. P., Clemmons, J. H., and Boehm, M. H.: 1991, *J. Geophys. Res.* **96**, 225.

- Feldman, W. C., Asbridge, J. R., Bame, S. J., and Montgomery, M. D.: 1973, *J. Geophys. Res.* **78**, 3697.
- Filbert, P. C. and Kellogg, P. J.: 1979, *J. Geophys. Res.* **84**, 1369.
- Frank, L. A.: 1969, *J. Geophys. Res.* **75**, 1269.
- Gloeckler, G., Hovestadt, D., and Fisk, L.A.: 1979, *Astrophys. J.* **230**, L191.
- Gosling, J. T., Asbridge, J. R., Bame, S. J., Feldman, W. C., Paschmann, G., and Sckopke, N.: 1980, *J. Geophys. Res.* **85**, 744.
- Gough, M. P.: 1985, *IEEE Trans. Geosci. Remote Sens.* **GE-23**, 305.
- Lin, R. P.: 1974, *Space Sci. Rev.* **16**, 189.
- Lin, R. P.: 1985, *Solar Phys.* **100**, 537.
- Lin, R. P. and Hudson, H. S.: 1971, *Solar Phys.* **17**, 412.
- Lin, R. P. and Hudson, H. S.: 1976, *Solar Phys.* **50**, 153.
- Lin, R. P. and Kahler, S. W.: 1992, *J. Geophys. Res.* **97**, 8203.
- Lin, R. P., Levendahl, W. K., Lotko, W., Gurnett, D. A., and Scarf, F. L.: 1986, *Astrophys. J.* **308**, 954.
- Lin, R. P., Potter, D. W., Gurnett, D. A., and Scarf, F. L.: 1981, *Astrophys. J.* **251**, 364.
- Paschmann, G., Sckopke, N., Asbridge, J. R., Bame, S. J., and Gosling, J. T.: 1980, *J. Geophys. Res.* **85**, 4689.
- Potter, D. W., Lin, R. P., and Anderson, K. A.: 1980, *Astrophys. J.* **236**, L97.
- Sarris, E. T., Krimigis, S. M., Bostrom, C. O., and Armstrong, T. P.: 1978, *J. Geophys. Res.* **83**, 4289.